



**HAL**  
open science

# Wave Kinematics in a Two-Dimensional Plunging Breaker

Yves-Marie Scolan, Pierre-Michel Guilcher

► **To cite this version:**

Yves-Marie Scolan, Pierre-Michel Guilcher. Wave Kinematics in a Two-Dimensional Plunging Breaker. Water Waves, 2019, 2 (2), pp.185-206. 10.1007/s42286-019-00013-w . hal-02304691

**HAL Id: hal-02304691**

**<https://ensta-bretagne.hal.science/hal-02304691>**

Submitted on 17 Sep 2021

**HAL** is a multi-disciplinary open access archive for the deposit and dissemination of scientific research documents, whether they are published or not. The documents may come from teaching and research institutions in France or abroad, or from public or private research centers.

L'archive ouverte pluridisciplinaire **HAL**, est destinée au dépôt et à la diffusion de documents scientifiques de niveau recherche, publiés ou non, émanant des établissements d'enseignement et de recherche français ou étrangers, des laboratoires publics ou privés.



Distributed under a Creative Commons Attribution 4.0 International License

# Wave Kinematics in a Two-Dimensional Plunging Breaker

Yves-Marie Scolan<sup>1</sup> · Pierre-Michel Guilcher<sup>1</sup>

Received: 22 January 2019 / Accepted: 12 July 2019 / Published online: 8 August 2019  
© Springer Nature Switzerland AG 2019

## Abstract

In the wake of theoretical, numerical and experimental advances by a large number of contributors, we revisit here some aspects of the fluid kinematics in a two-dimensional plunging breaker occurring in shallow water. In particular, we propose a simplified identification of the velocity distribution at the free surface in terms of the velocity at some characteristic points. We can then simply explain the reasons for which the velocity is maximum inside the barrel at its roof. We also show that the relative velocity field calculated in a coordinate system centered to a point where the velocity is maximum may have a possible analytic representation.

**Keywords** Potential flow · Nonlinear wave kinematics · Plunging breaker

## 1 Introduction

The kinematics in the fluid of a plunging breaker has been abundantly studied in the past. The pioneering works by John [13] for the theoretical developments and by Miller [18] for the experimental observations are often cited in the papers that appeared in 70s and early 80s. The literature on the kinematics in breaking waves became more and more abundant as soon as the available computational resources have yielded the first numerical results with robust enough algorithms. The corresponding numerical models appeared in the late 70s and early 80s; they were mainly formulated in Potential Theory for two-dimensional configurations. Since the pioneering works by Longuet-Higgins and Cokelet [16], Vinje and Brevig [28] and Dold and Peregrine [8], many studies have been achieved. Since then, Potential Theory remains undoubtedly the right framework to analyse the fine details of a breaker as long as no rotational effects predominate (see [12]). Indeed, that is the case during the early stages of the flow in a

---

✉ Yves-Marie Scolan  
yves-marie.scolan@ensta-bretagne.fr

Pierre-Michel Guilcher  
pierre-michel.guilcher@ensta-bretagne.fr

<sup>1</sup> ENSTA Bretagne IRDL UMR 6027, 2 Rue François Verny, 29806 Brest Cedex 9, France

sloshing tank as shown in Karimi et al. [14]. Obviously, when dealing with overturning crest thus leading to an entrapped gas pocket, it is a drastic approximation to neglect the influence of the gas dynamics above the liquid. Indeed, the obtained results must always be commented having in mind how these results will be influenced by the presence of gas which interacts more or less strongly with the liquid provided that both fluids (liquid and gas) are non-miscible. Since the recent work by Song and Zhang [26], we know that the inner surface of the gas pocket may have complicated shape. Before that, it is also observed that the formation of the pocket close to wall is delayed by the presence of the entrapped gas and the crest is much less sharp due to the strong gas flow occurring when the pocket closes up, the gas being compressible or not. For low density ratio (about  $10^{-3}$  like water/air), this phenomenon is commented in Guilcher et al. [11], Scolan et al. [21] and Etienne et al. [10]. In the present study, the liquid is covered with vacuum and the free surface is hence an isobar surface.

Nowadays, the modelling of overturning crest can be done routinely in the frame of Potential Theory. Hence, parametric studies can be carried out to catch highly nonlinear behavior of the free surface. In particular, we are concerned with highly energetic waves. Indeed, when waves break, the breaker concentrates a large amount of kinetic energy. At the free surface, where the pressure is constant, we observe a competition between inertia effects represented by the time derivative of the velocity potential and the gradient square of the same velocity potential. Both terms are opposite in sign. Therefore, when concentration of one of them occurs close to the free surface, it is counterbalanced with an increase of the other as long as gravity effects do not play the main role. It is observed that in the vicinity of the crest we can detect such phenomena. That is the purpose of the present article to investigate some aspects of the wave kinematics whereas an overturning crest develops. The numerical tool which yields the results belong to the class of desingularized models for two-dimensional configurations (see [27]). Using conformal mappings of the fluid domain, only the free surface needs to be discretized thus reducing drastically the number of unknowns. Most of the time, the present model is robust enough to avoid the use of any smoothing or even regriding. The model is described in Scolan [20] and the latest developments are detailed in Scolan and Brosset [22]. Appendix A gives the outlines of the method: governing equations, numerical parameters, accuracy checking and the most recent validation tests.

The present paper is organized as follows. Section 2 draws the main features of an overturning crest in an almost open sea. The kinematics in the wave (velocity and acceleration) are described both in terms of their distribution and amplitude. Comparisons are presented between shallow water and deep water plunging breaker. An identification is performed in Sect. 3 between the velocity components (normal and tangential) in terms of horizontal velocities calculated at some characteristic points. In Sect. 4, the velocity in the plunging crest is analysed in a relative coordinate system centered at the point where the velocity is maximum in the fluid. It is shown that the complex potential that represents a shear flow fits the resulting velocity field. Section 5 concludes that the computed wave kinematics does not allow to reach a high enough level of stored kinetic fluid energy. It then introduces the main challenges of the companion paper where it is intended to produce critical jets about a similar plunging breaker but with much more stored energy.

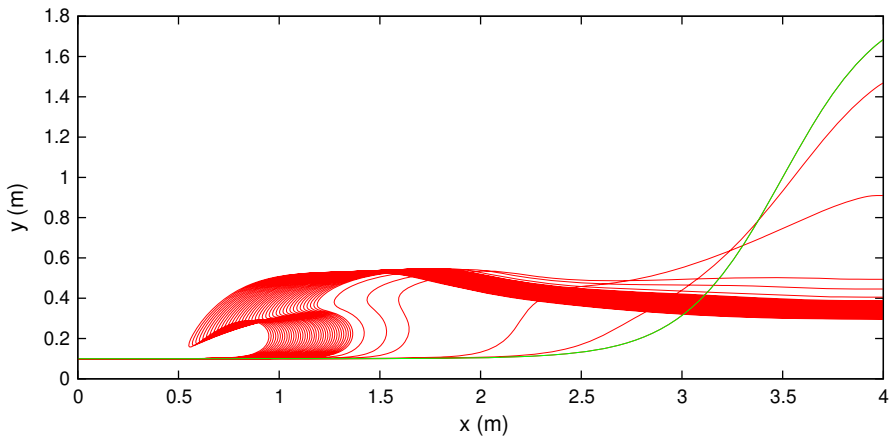
## 2 Standard Breaker in an (Almost) Open Sea

Figure 1 shows the successive free surface profiles obtained by solving the two-dimensional fully nonlinear potential flow problem when starting from an initial free surface deformation. The free surface profiles are drawn in a coordinate system centered at the left bottom corner of the tank. The initial free surface is of Gaussian type:  $y = h + ae^{-r(x-L)^2}$  with  $L = 4$  m (length of the tank),  $h = 0.2$  m depth,  $a = 0.9$  m,  $r = 2$  m<sup>-2</sup>. For the present simulation, 300 markers are used and they are uniformly distributed along the initial free surface profile. The time steps are refined as the crest overturns: initial time step  $\Delta t = 0.01$  s,  $\Delta t = 0.001$  s when  $t > 0.8$  s,  $\Delta t = 0.0001$  s when  $t > 0.9$  s. That configuration can be considered as a typical dam-breaking problem. We hence consider a configuration where the influence of the left wall is not significant, that is why it is denoted “an almost open sea”. If the initial potential energy is great enough, the resulting free surface flow can lead to a breaker of different types. The present breaker is a plunging breaker and in this paper we shall focus on this kind of breaking wave only. In particular, we analyze in more detail the distribution of velocity and acceleration in the fluid and at the free surface. To describe the spatial variation of the kinematics, we use the arc length  $\sigma$ . It is measured along the free surface positively from the left wall as illustrated in Fig. 2. The arc length of the crest tip is denoted  $\sigma_{\text{tip}}$ . The terminology, convention and notations are given in Fig. 3. The specific shape of a plunging breaker enables to distinguish four points on the free surface where the tangent is either horizontal (points 2 and 3) or vertical (points 1 and 4). The spatial variations of the curvature radius and the Cartesian components of the tangent for the free surface profile drawn in Fig. 3 are typical of an overturning crest in shallow water depth. One of the common features of plunging breaker is that the region of maximum of velocity is in the vicinity of the crest. Consistent with the computations of New [19], Dommermuth et al. [9] and Yasuda [29], it is observed that the maximum velocity does not occur exactly at the tip of the overturning crest. In fact, that maximum is located along the lower part of the breaker at an intermediate distance between the crest and the point where the slope of the free surface is vertical. Figure 4 is a closer view of the plunging jet shown in Fig. 1. Superimposed curves allow to follow the tip of the crest and the location of the maximum of the velocity (its magnitude). To better distinguish these two locations in time and space, we plot in Fig. 5 the modulus of the velocity  $||\vec{u}|| = ||\vec{\nabla}\phi||$  in terms of time  $t$  and arc length  $\sigma$ . It should be noted that the regularity of the mesh is a consequence of the accuracy and robustness of the computational code. The obtained surface drawn in the space  $(t, \sigma)$  is hence structured. As a consequence, a line parametrized by time  $t$  corresponds to the time variation of the arc length of a given marker throughout the whole simulation. It is hence remarkable that the code concentrates (automatically) the markers where it is necessary, that is to say where the radius of curvature becomes small (tip of the crest, for example). The arc length of the maximum velocity is denoted  $\sigma_{u_{\text{max}}}$ . The superimposed curves follow the maximum of the velocity and the crest (that is the point where the velocity potential reaches its maximum, alternatively the tangential velocity changes sign). It is observed that the velocity will never be greater than a threshold. In the present case,  $u_{\text{max}} \approx 4$  m/s, which is approximately twice a phase velocity  $\sqrt{gA}$  calculated with an amplitude  $A \approx 0.4$  m, that is, to say the height of

the front which is formed after the collapse of the fluid mass. Figure 5 also shows that the velocity does not vary much between the two arc lengths  $\sigma_{\text{tip}}$  and  $\sigma_{u_{\text{max}}}$ . It is also clear that, as we approach the end of the simulation, the maximum of velocity is not at the tip of the crest any longer.

### 3 Identification of the Velocity at the Free Surface

Once the plunging tip has appeared, the shape of the breaker remains quite standard and the corresponding kinematics as well. To confirm that, we plot the spatial variation of the velocity components along the free surface. Figure 6 shows the variation of the Cartesian components and the normal and tangential velocities as well, at an instant ( $t = 0.848$  s) when the plunging breaker is well developed (same shape than in Fig. 3). These are the components of the Lagrangian velocity, that is to say, the velocity which is used to transport the markers of the free surface. The horizontal velocity is maximum at point 2, while the vertical velocity vanishes at the same point 2. It is noticeable that the tangential velocity is more important than the normal velocity.



**Fig. 1** Dam breaking case: successive free surface profiles (red lines). One profile over 20 is plotted. Initial time step  $\Delta t = 0.01$  s,  $\Delta t = 0.001$  s when  $t > 0.8$  s,  $\Delta t = 0.0001$  s when  $t > 0.9$  s. Number of markers: 300. initial free surface deformation (green line) of Gaussian type :  $y = h + ae^{-r(x-L)^2}$  with  $L = 4$  m (length of the tank),  $h = 0.2$  m,  $a = 0.9$  m,  $r = 2 \text{ m}^{-2}$  (color figure online)

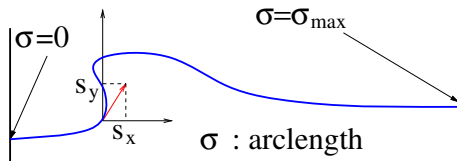


**Fig. 2** Convention and notation of the arc length used to describe the spatial variation along the free surface. The arc length  $\sigma$  is measured positively from the left wall to the right wall. The Cartesian components of the tangent vector are denoted  $(s_x, s_y)$

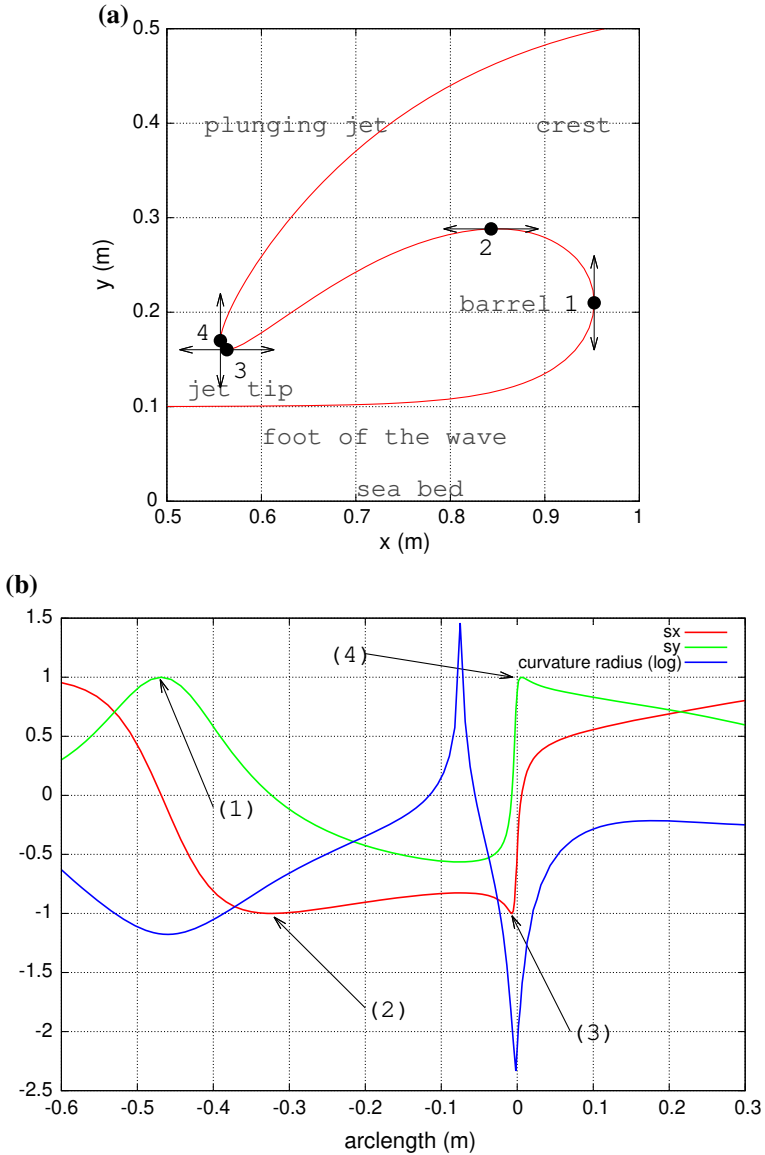


**Fig. 3** **a** Terminology used to describe the plunging breaker. The arrows distinguish four geometric points on the free surface where the tangent is either horizontal (points 2 and 3) or vertical (points 1 and 4). **b** Spatial variation of the curvature radius ( $\log_{10}$ ) and the Cartesian components ( $s_x, s_y$ ) of the tangent with the arc length  $\sigma$  and the origin centered at the arc length of the tip  $\sigma_{\text{tip}}$ . Those data correspond to the free surface profile drawn in **a**. The origin of the arc length is centered at the tip of the crest. See Fig. 1 for computational data. The units are meters (m)

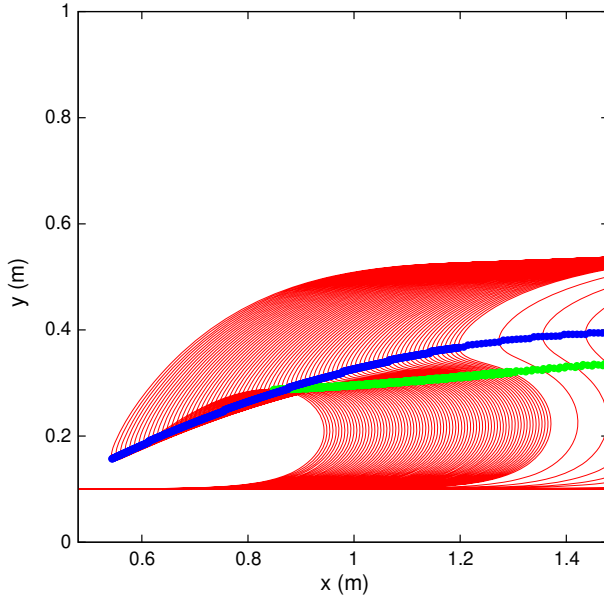


**Fig. 4** Closer view of the plunging breaker at time  $t = 0.848$  s. Blue marks: tip of the crest, green marks: maximum of velocity modulus on each free surface profile. See Fig. 1 for computational data (color figure online)

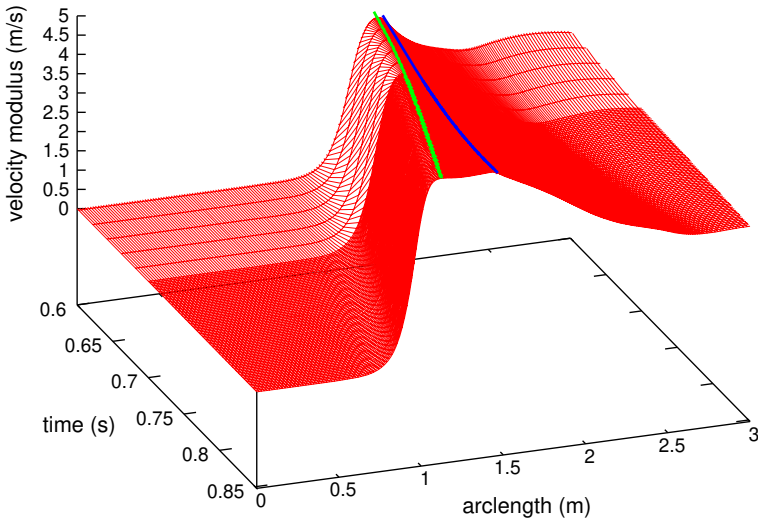


**Fig. 5** Variation of the velocity modulus  $||\vec{\nabla}\phi||$  in terms of time  $t$  and arc length  $\sigma$  along the free surface with origin at the left wall. Superimposed blue curve: location of the crest, superimposed green curve: location of the maximum velocity. See Fig. 1 for computational data. The unit of the velocity is m/s (color figure online)

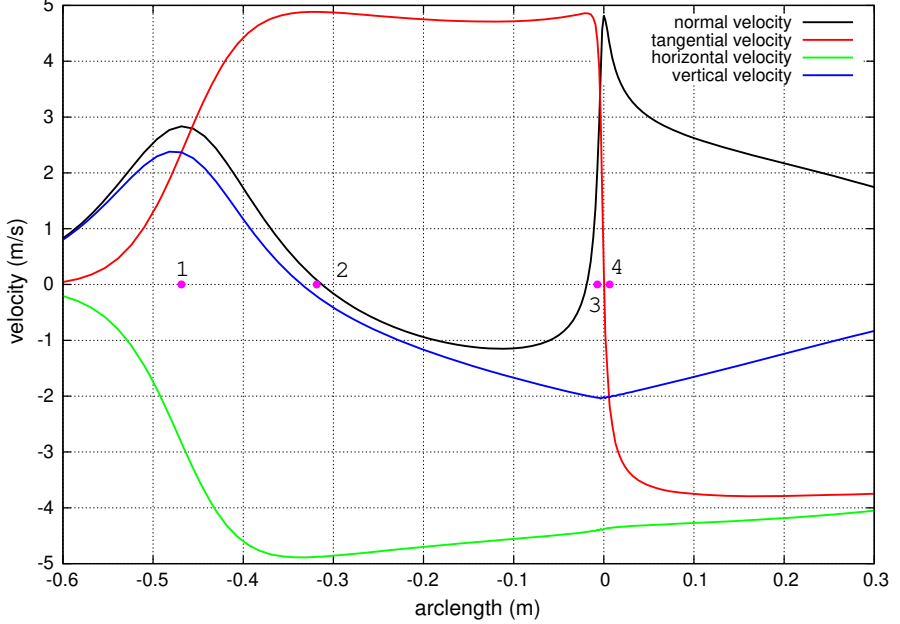


**Fig. 6** Spatial variation of the velocity components: Cartesian horizontal and vertical ( $U$ ,  $V$ ), respectively, normal velocity ( $\phi_n$ ) and tangential velocity ( $\phi_s$ ) components for the breaker shown in Fig. 3 at instant  $t = 0.848$  s. The origin of the arc length  $\sigma$  is centered at the arc length of the tip  $\sigma_{\text{tip}}$ . The arc length of points 1, 2, 3 and 4 (see Fig. 3) are emphasized with marks on the horizontal axis. See Fig. 1 for computational data. The unit of the velocity is m/s

The tangential velocity slightly varies between  $\sigma_{\text{tip}}$  and  $\sigma_{u_{\text{max}}}$ . Within that interval, the normal velocity changes sign in the close vicinity of  $\sigma_{u_{\text{max}}}$ . If we denote  $U_2$  and  $U_1$  the instantaneous horizontal velocity at points 2 and 1, respectively, we can proceed by identification between  $-U_1 s_y$  and the normal velocity  $\phi_n$  on the one hand and between  $\frac{1}{2}U_2(s_x - 1)$  and the tangential velocity  $\phi_s$ , on the other hand. That is shown in Fig. 7. This identification follows from a simple observation of the temporal and spatial variations of the variables. This identification works satisfactorily inside the barrel, that is to say, when  $\sigma < \sigma_{\text{tip}}$ . In other words, the kinematics on the free surface is governed by the inner shape of the breaker. It is questionable whether or not that is true over time. Figure 8 shows the same identification as the breaker develops. Indeed, the kinematics in the barrel is mainly governed by the shape and the velocity at two specific points. Over time, the validity of those approximations are reasonable as long as  $U_2$  and  $U_1$  do not vary much over time. This result is also clearly valid for shallow depth. Its extension to deep water is more questionable. However, at that stage it is remarkable to conclude that the size of the plunging breaker determines the fluid kinematics. This conclusion was also formulated in the past by New [19].

The analysis of the velocity distribution yields the location of the maximum horizontal velocity. We plot in Fig. 9 the temporal variations of two characteristic arc lengths:  $\sigma_2$  the arc length of point 2 where  $s_y = 0$ , and the arc length of the point where the horizontal velocity is maximum. It is shown that these two arc lengths coin-

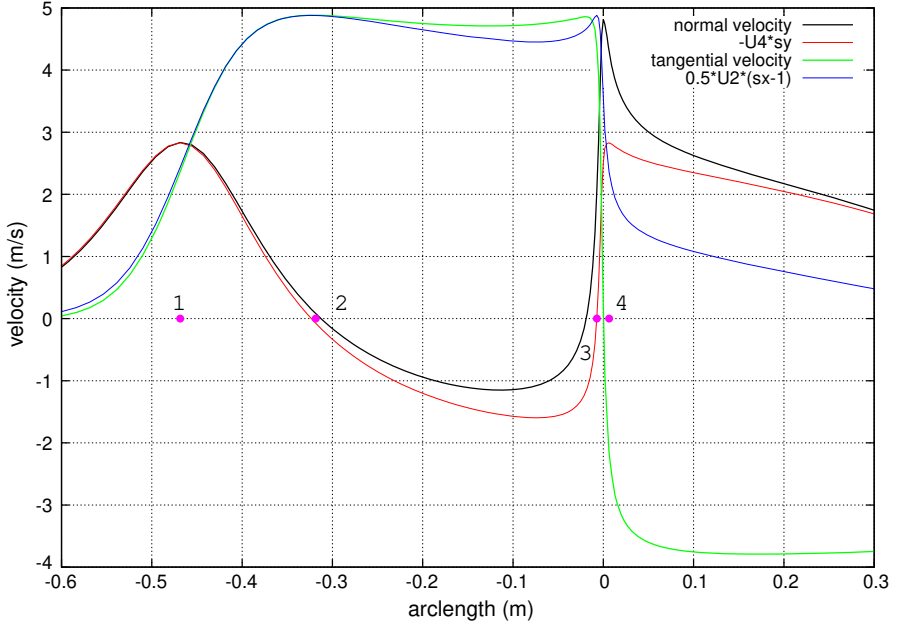


**Fig. 7** Identification between  $-U_4s_y$  and the normal velocity  $\phi_n$  and between  $\frac{1}{2}U_2(s_x - 1)$  and the tangential velocity  $\phi_s$  at instant  $t = 0.848$  s. The arc length of points 1, 2, 3 and 4 (see Fig. 3) are emphasized with marks on the horizontal axis. See Fig. 1 for computational data. The unit of the velocity is m/s (color figure online)

cide as soon as the barrel is formed. It is questionable whether or not that is true for another breaker, in particular, when the depth increases. Figure 10 describes that case. The initial free surface deformation is of Gaussian type:  $y = h + ae^{-r(x-L)^2}$  with  $L = 4$  m,  $h = 2$  m,  $a = 2.7$  m,  $r = 2\text{m}^{-2}$ . The initial time step is  $\Delta t = 0.01$  s, then  $\Delta t = 0.001$  s when  $t > 0.6$  s, and finally  $\Delta t = 0.0001$  s when  $t > 0.7$  s. The number of markers is 400. Figure 10c confirms that the characteristics observed for shallow water plunging breaker are still true for a plunging breaker in a great water depth, even if there is a significant global vertical velocity of the crest.

In terms of acceleration, Fig. 11 shows the modulus of the Lagrangian acceleration  $\frac{d\vec{\nabla}\phi}{dt}$  in terms of time  $t$  and arc length  $\sigma$ . Their calculations follow from a first-order time finite difference of the Lagrangian velocity of the markers. Superimposed curves allow to follow the tip of the crest, the location of the maximum of the velocity and the maximum of acceleration. As the crest is starting to overturn, the location of the maximum acceleration occurs in a close vicinity of the point where the slope of the free surface is vertical, which is in agreement with the conclusion of Skyner [25] and Yasuda [29]. This is confirmed by Fig. 12 which shows the free surface profile around the overturning crest and the location of the maximum acceleration on each profile. Figure 13a shows the spatial variation of the acceleration components along the free surface in the barrel from the foot to the tip of the crest. The chosen instant is  $t = 0.848$  s, this is the same as in Figs. 3 and 6. The acceleration components are

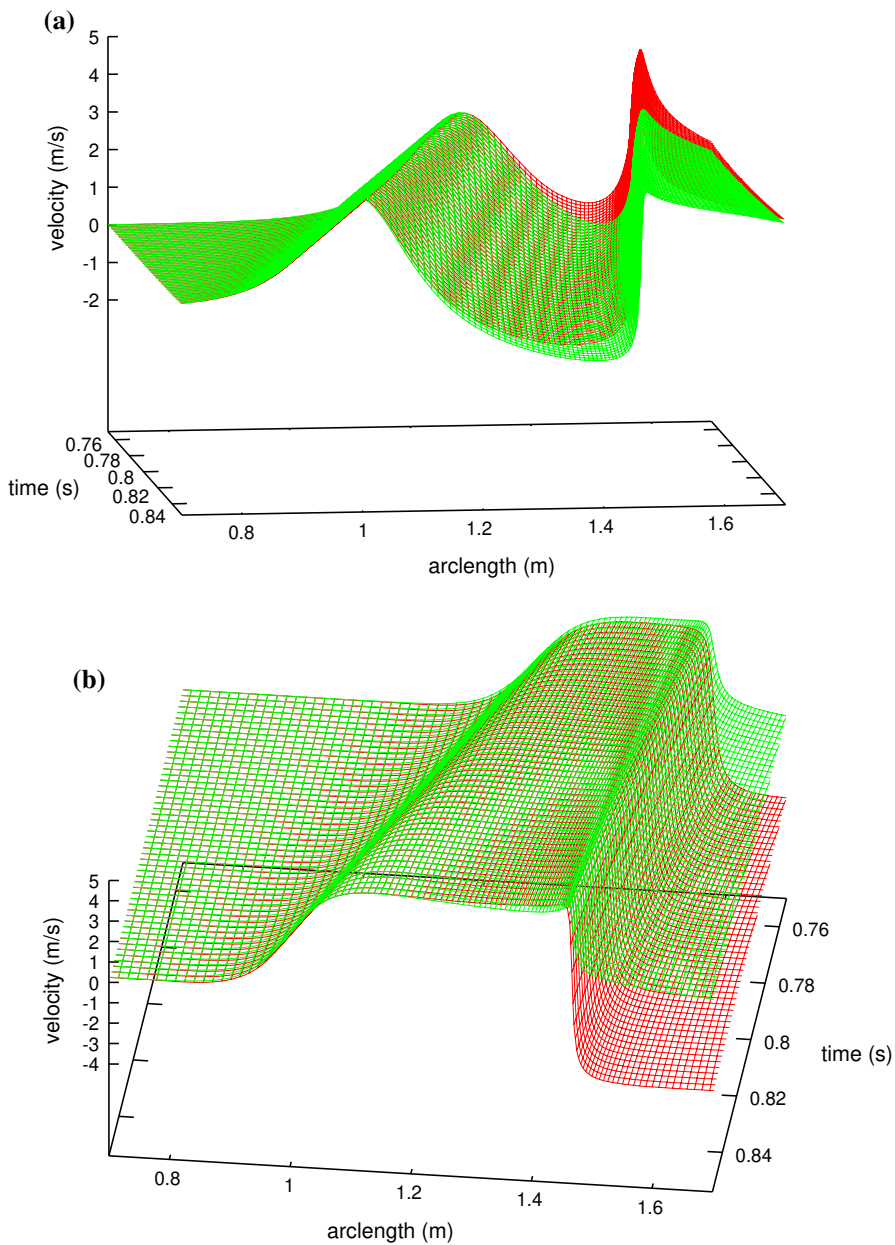


**Fig. 8** **a** Identification over time ( $t$ ) and space ( $\sigma$ ) between  $-U_1(t)s_y$  and the normal velocity  $\phi_{,n}$ . **b** Identification over time ( $t$ ) and space ( $\sigma$ ) between  $\frac{1}{2}U_2(t)(s_x - 1)$  and the tangential velocity  $\phi_{,s}$ . The numerical data are plotted in red. The approximated formulae are plotted in green. See Fig. 1 for computational data. The unit of the velocity is m/s (color figure online)

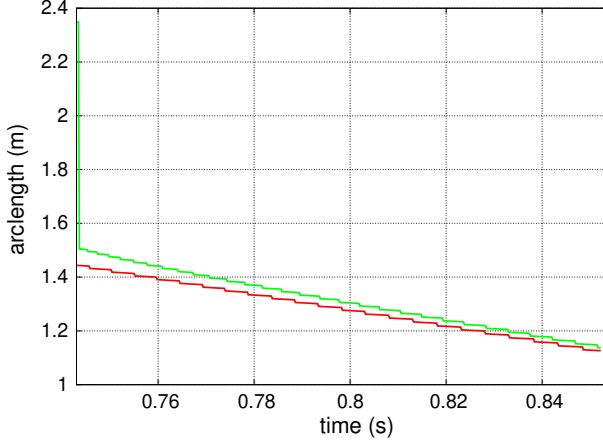


**Fig. 9** Temporal variations of two characteristic arc lengths:  $\sigma_2$  arc length of point 2 (green) where  $s_y = 0$ ,  $\sigma_{u_{\max}}$  the arc length where the horizontal velocity is maximum (red). Before  $t \approx 0.743$  s, point 2 does not exist yet. See Fig. 1 for computational data (color figure online)

made non-dimensional with the acceleration of gravity  $g = 9.81 \text{ m/s}^2$ . The maximum acceleration (here about 9 times the gravity) occurs in a close vicinity of the point 1 where the radius of curvature in the barrel is the minimum. At that point, the vertical acceleration changes sign while the horizontal component is maximum (negative).

Some properties of the acceleration (and velocity) fields follow directly from the analysis of Euler's equations. Conservation of momentum links the Lagrangian acceleration of a fluid particle to the pressure gradient and gravity as follows:

$$\frac{d\vec{u}}{dt} = -\frac{1}{\rho}\vec{\nabla}p + \vec{g}. \quad (1)$$

The Cartesian components of the velocity  $\vec{u}$  are denoted ( $U$ ,  $V$ ). Table 1 summarizes the values of the horizontal and vertical accelerations at the four characteristic points ranged as the arc length  $\sigma$  increases from point #1 to point #4.

We use the theoretical result that  $p_{,n}$  is always negative at the free surface (see [7]) As a consequence, the modulus of the Lagrangian acceleration is always greater at point 3 than at point 4 as long as the normal gradient of the pressure does not vary much between the two points 4 and 3. We can certainly prove that  $|p_{,n}/\rho|$  almost vanishes at the crest since the fluid at the tip is in free fall (accelerated by the gravity only). Figure 13b shows the spatial variation of  $|p_{,n}/\rho|$  along the free surface and confirms this result. The fluid hence decelerates more along the upper face of the crest than along the inner face of the barrel. As a consequence, since the horizontal velocities at points 4 and 3 are quite similar, it is expected that  $|U_4| < |U_3|$ . It should be noted that in the present configuration depicted in Fig. 1,  $U < 0$  all over the fluid in the crest.

Between the points 3 and 2, where the horizontal acceleration is necessarily small since nil at the points 3 and 2, we also expect a slight variation of the horizontal component of the velocity. Since the variation along the arc length  $\sigma$  is such that  $|U|$

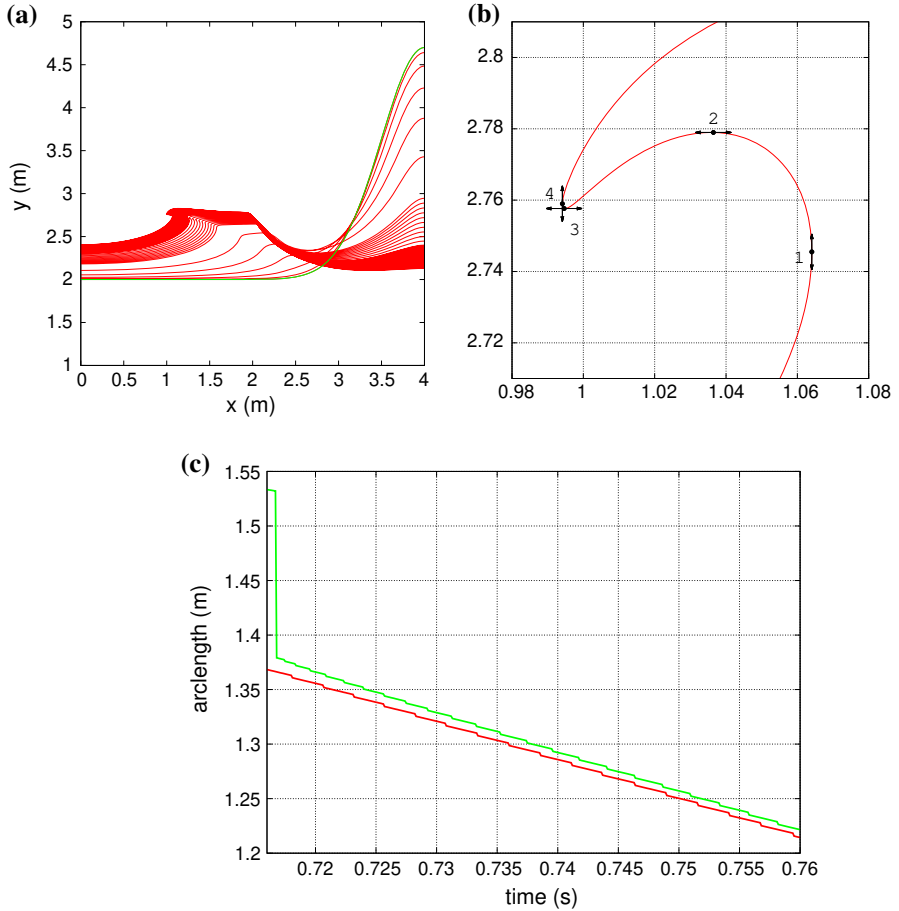


**Fig. 10** Dam breaking case leading to a plunging breaker: **a** successive free surface profiles (red lines) and initial free surface deformation (green line) of Gaussian type :  $y = h + ae^{-r(x-L)^2}$  with  $L = 4m$  (length of the tank),  $h = 2m$ ,  $a = 2.7m$ ,  $r = 2m^{-2}$ . **b** Characteristics points along the free surface profile corresponding to instant  $t = 0.76s$ , see notation in Fig. 3, **c** temporal variations of two characteristic arc lengths:  $\sigma_2$  arc length of point 2 (green) where  $s_y = 0$ ,  $\sigma_{U_{\max}}$  the arc length where the horizontal velocity is maximum (red). Before  $t \approx 0.717s$ , point 2 does not exist yet (color figure online)

goes on increasing as we approach the point 2, and given that the horizontal velocity  $|U|$  decreases dramatically at point 1, the maximum necessarily occurs in the vicinity of point 2. These results are quite in line with those of Constantin [6].

We can analyze more deeply the kinematics inside the plunging breaker. In Fig. 14, we plot the isolines of the pressure components  $-\phi_{,t}$  and  $\frac{1}{2}\nabla\phi^2$  in the crest at the last computed instant  $t = 0.852s$ . These two components increase smoothly from the foot of the breaker to the tip of the crest. The regularity of the isolines in Fig. 14 illustrates that monotonicity. We can observe that the region of maximum inertia term

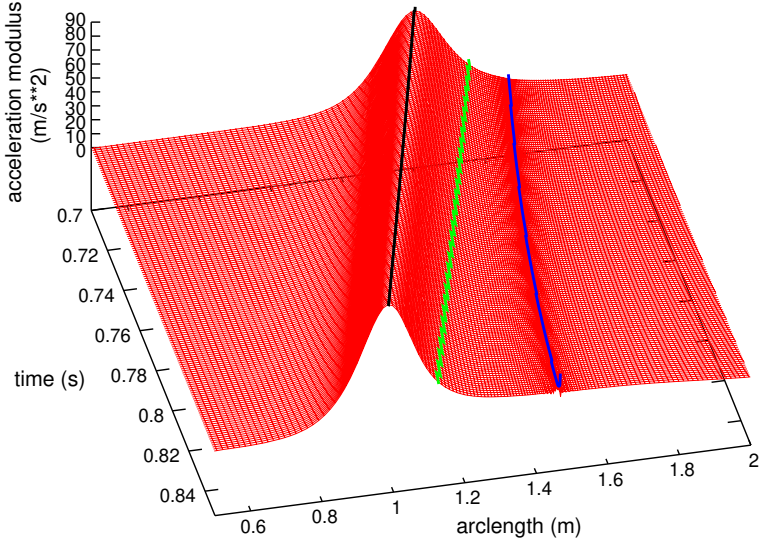


**Fig. 11** Variation of the Lagrangian acceleration  $\frac{d\vec{v}}{dt}$  (modulus) at the free surface in terms of time  $t$  and arc length  $\sigma$ . Superimposed blue curve: location of the crest, superimposed black curve: location of the maximum acceleration, and superimposed green curve: location of the maximum velocity. See Fig. 1 for computational data. The unit of the acceleration is  $\text{m/s}^2$  (color figure online)

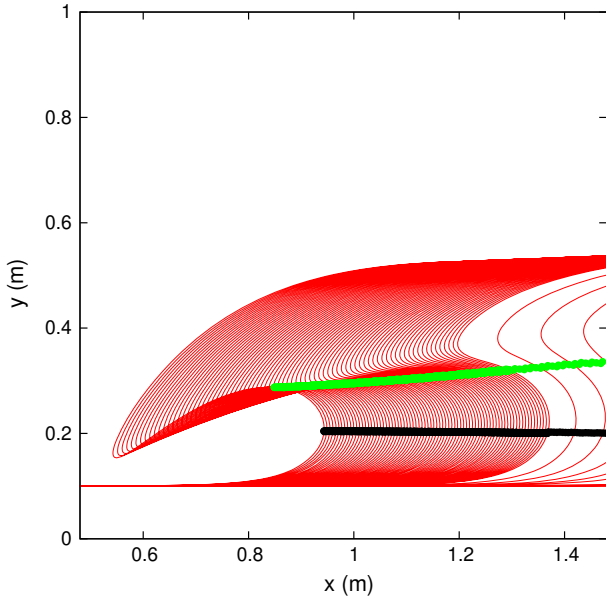


**Fig. 12** Closer view of the plunging breaker. Superimposed green dots: maximum velocity, and superimposed black dots: maximum acceleration. See Fig. 1 for computational data (color figure online)

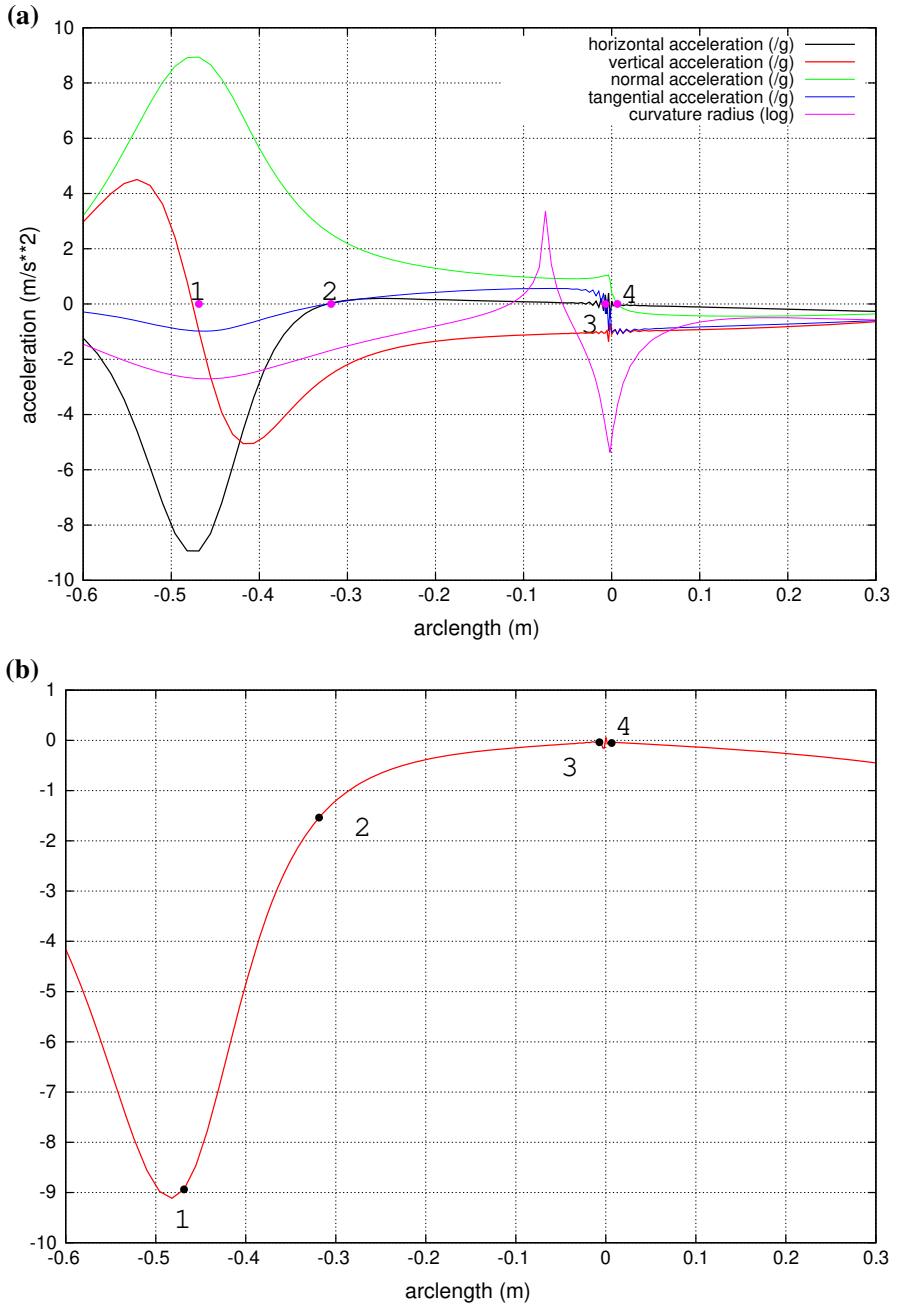


**Fig. 13** **a** Spatial variation of the acceleration components: Cartesian horizontal and vertical component of the acceleration ( $\dot{U}$ ,  $\dot{V}$ ), normal and tangential components along the free surface (made non-dimensional with the acceleration of gravity  $g$ ). **b** Spatial variation of the normal gradient of the pressure (divided by  $\rho g$ ) along the free surface. Same breaker as the one shown in Fig. 3 at instant  $t = 0.848$  s. The arc lengths of points 1, 2, 3 and 4 (see Fig. 3) are emphasized with marks on the horizontal axis or on the curve. The origin of the arc length is centered at the tip of the crest. See Fig. 1 for computational data

**Table 1** Tangential, normal, horizontal and vertical accelerations at the four characteristics points ranged as the arc length  $\sigma$  increases from point #1 to point #4

Point #	1	2	3	4
$\frac{d\vec{u}}{dt} \cdot \vec{s}$	$-g$	0	0	$-g$
$\frac{d\vec{u}}{dt} \cdot \vec{n}$	$-p,n/\rho$	$-p,n/\rho + g$	$-p,n/\rho + g$	$-p,n/\rho$
$\frac{dU}{dt}$	$p,n/\rho$	0	0	$p,n/\rho$
$\frac{dV}{dt}$	$-g$	$p,n/\rho - g$	$p,n/\rho - g$	$-g$

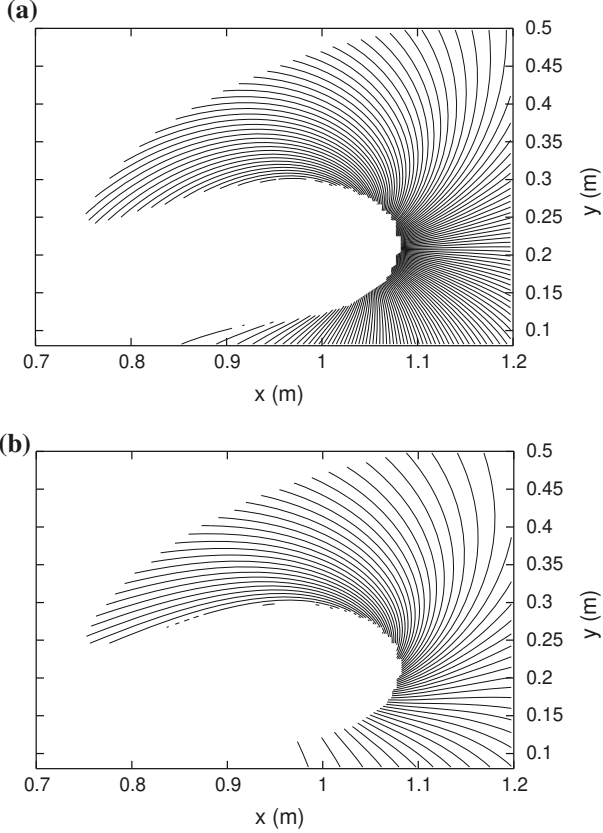


**Fig. 14** **a** Isolines of  $-\phi,t$  and **b** isolines of  $\frac{1}{2}\vec{\nabla}\phi^2$  at instant  $t = 0.852$  s. See Fig. 1 for computational data. Each isoline corresponds to a constant value of the variable. The step between each isoline is  $0.1\text{m}^2/\text{s}^2$ . The magnitudes of  $-\phi,t$  and  $\frac{1}{2}\vec{\nabla}\phi^2$  increase from the foot to the crest

$-\phi,t$  surrounds the point  $\sigma_{u_{\max}}$  while the region of maximum kinetic energy  $\frac{1}{2}\vec{\nabla}\phi^2$  extends from  $\sigma_{u_{\max}}$  to  $\sigma_{\text{tip}}$ . The accumulation of kinetic energy around the point  $\sigma_{u_{\max}}$  is hence associated with an increasing acceleration of the fluid somewhere in that area.

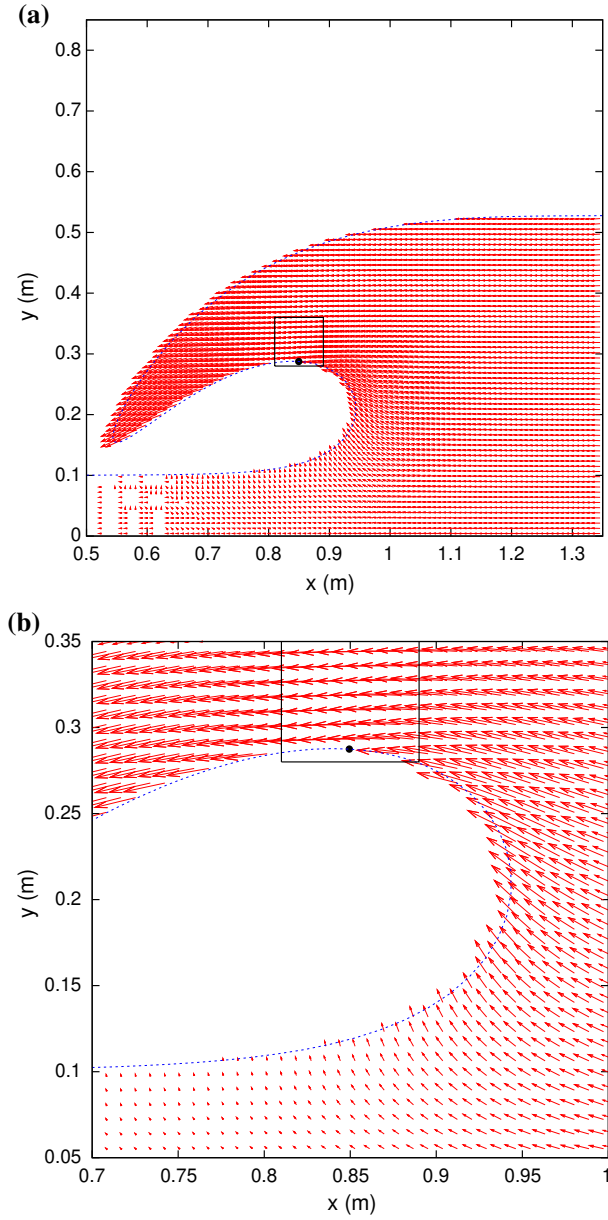


**Fig. 15** Velocity field in the overturning crest at the final instant of computation. **a** Global view, **b** closer view. The black dot indicates the point where the velocity is maximum. The unit of length is m. The vector length is divided with factor 200. The frame indicates the frame of the closer view in Fig. 16

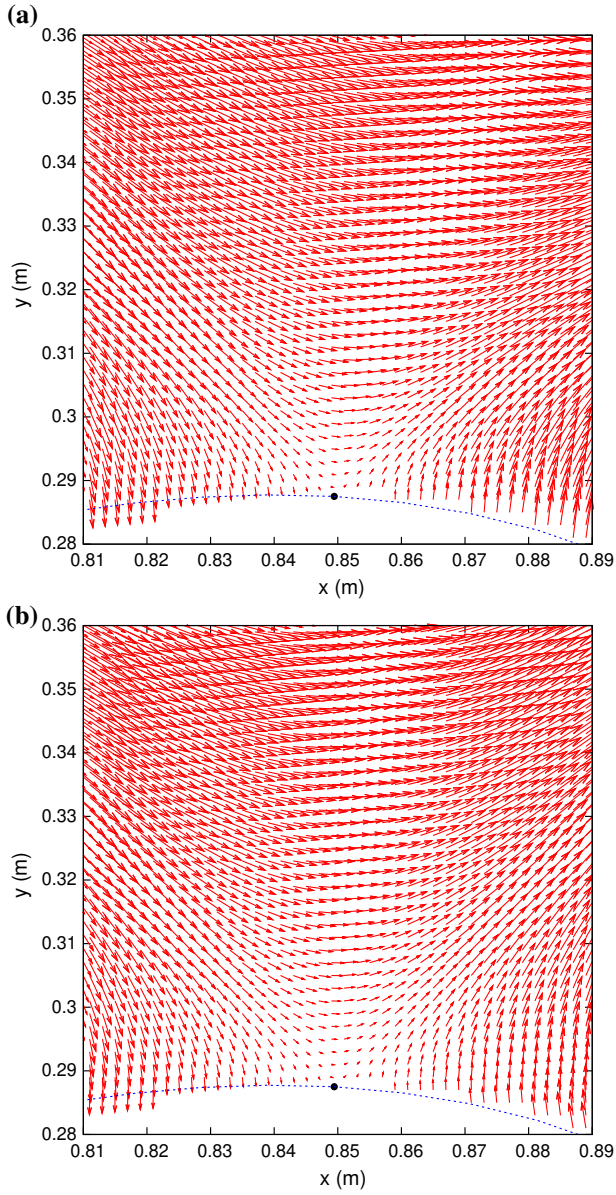


**Fig. 16** Closer view of the velocity field about the point where the velocity is maximum denoted  $u_{max}$ . **a** Numerical velocity field  $\vec{u}$  from which the maximum velocity  $u_{max}$  is subtracted. The vector length is divided with factor 100. **b** Theoretical velocity field obtained from formula (3). The vector length is divided with factor 20

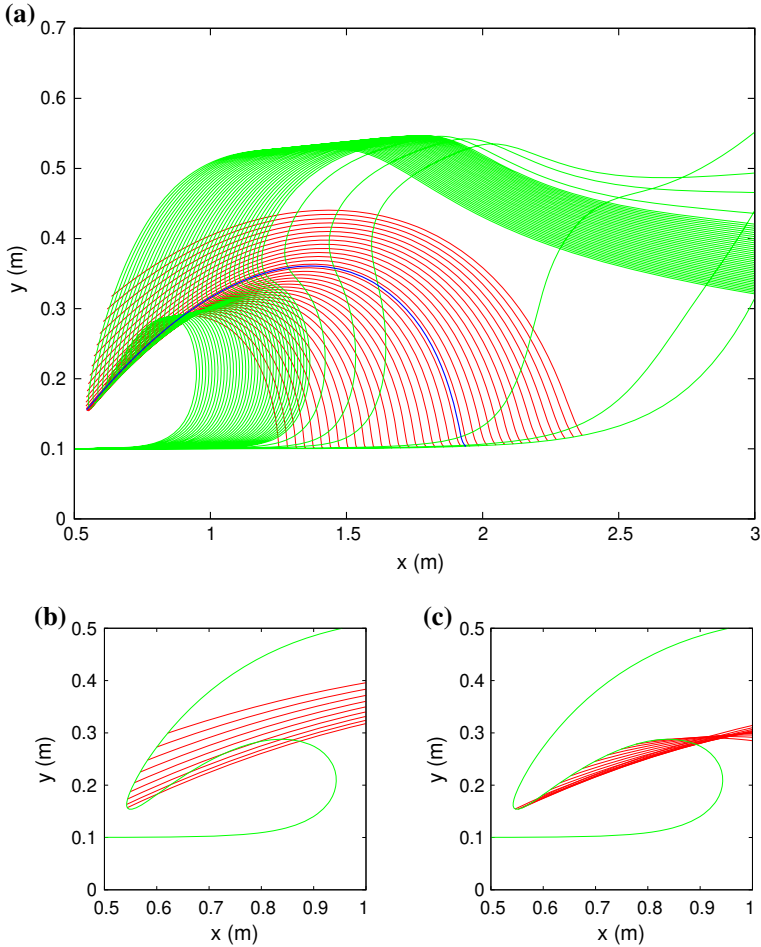


**Fig. 17** Trajectories of the Lagrangian markers and free surface profiles. One trajectory over two is plotted. One profile over 20 is plotted. **b, c** The last computed profile at instant  $t = 0.8522$  s is plotted. See Fig. 1 for computational data

#### 4 Identification of the Velocity Field in the Plunging Crest

The analysis of the velocity field in the crest can be pursued in the light of the work done by Longuet-Higgins [17]. Figure 15 shows the velocity field in the overturning crest at an instant when the plunging jet is well developed. We identify the maximum velocity along the free surface and localize this maximum in the total velocity field. It is noticeable that the maximum velocity computed along the free surface is also the maximum velocity in the whole velocity field. To evaluate the different velocity components, we subtract the maximum velocity to the total velocity field. It is remarkable how the corresponding velocity field (plotted in Fig. 16) looks like a shear flow. The corresponding field can be represented using a complex potential. In an earth fixed coordinate system, a possible expression of that flow is

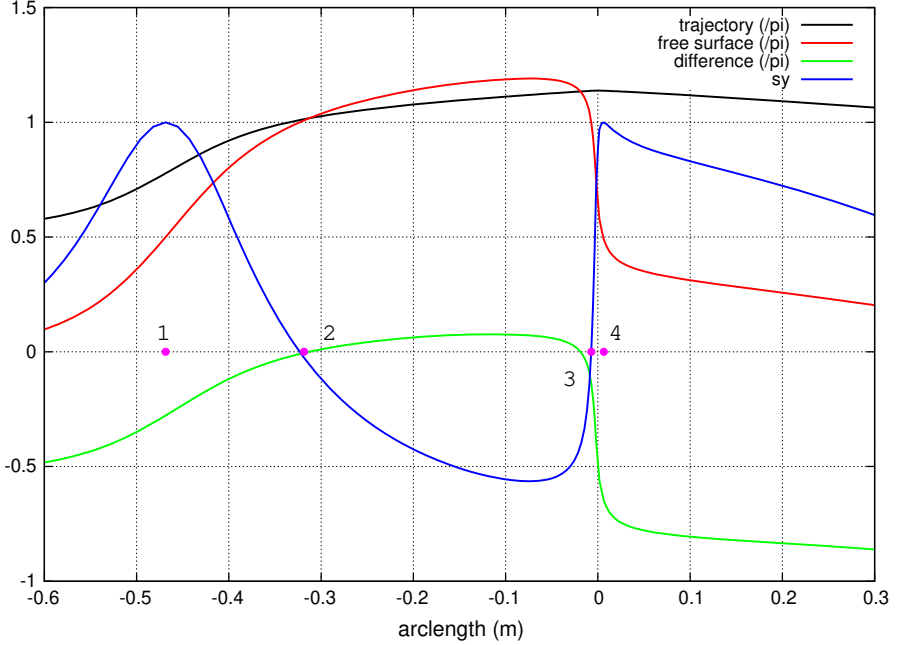


**Fig. 18** Variation of the angles made with the horizontal axis  $x$ , of the free surface (red) and the trajectory of markers (black) at instant  $t = 0.848$  s. The difference of these two angles is plotted in green. The angles are made nondimensional with  $\pi$ . The arc lengths of points 1, 2, 3 and 4 (see Fig. 3) are emphasized with marks on the horizontal axis. See Fig. 1 for computational data (color figure online)

$$F(z, t) = a(z - z_m(t))^2, \quad a \in \mathbb{C}, \quad (2)$$

where  $z_m(t)$  is the complex coordinate of the point where the velocity is maximum. As observed previously that point evolves over time. In the present case, we can set  $a = -iA$  and the real parameter  $A$  varies slowly over time. From the complex potential (2), we determine the corresponding velocity field from

$$w(z, t) = \frac{dF}{dz} = 2a(z - z_m(t)). \quad (3)$$

That velocity field is plotted in Fig. 16. Obviously the solution (2) does not meet the boundary conditions of the free surface problem. Following [17], the full complex potential should verify the conditions  $p = 0$  and  $\frac{dp}{dt} = 0$  on the free surface.

An interesting feature of the plunging breaker is illustrated in Fig. 17. We superpose the trajectories of the Lagrangian markers with the free surface profiles. Such plots are available because of the robustness of the code that does not require any regridding of the free surface (as reminded in Sect. 1). The general view (Fig. 17a) collects the data from the initial time of the simulation. It is shown from which fluid particles the tip of the plunging jet is made of. These results are quite in line with the experimental observations yielded by a Particle Image Velocimetry, as shown in Kimmoun et al. [15]. In the closer views (Fig. 17b, c), we distinguish the markers on each sides of the

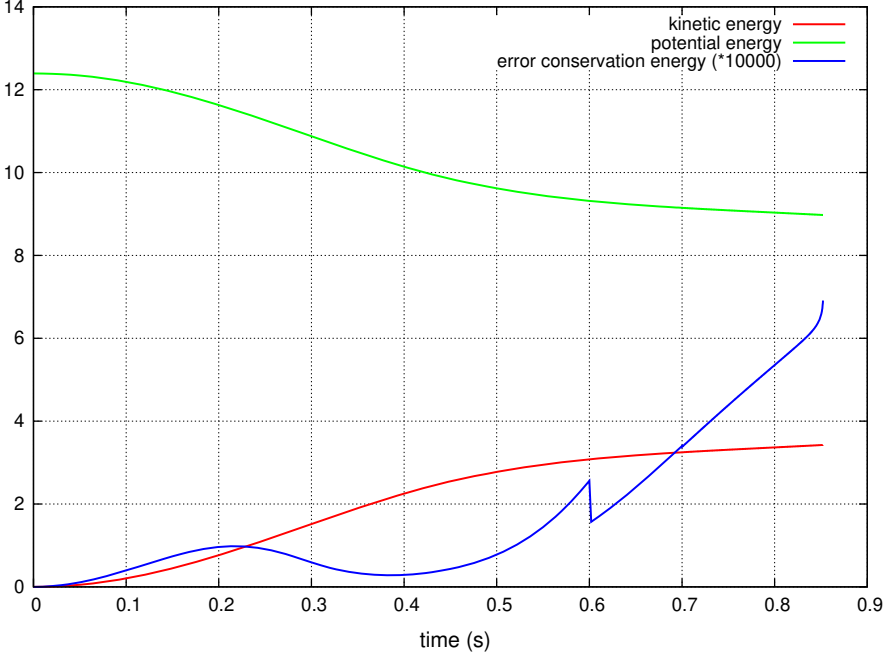


**Fig. 19** Time variation of the fluid energy components, potential energy: green line; kinetic energy: red line, error on the energy conservation (with factor  $10^4$ : blue line). The components of fluid energy are divided with the fluid density  $\rho$ . See Fig. 1 for computational data (color figure online)

crest. It is worth examining how the free surface intersects the trajectories. We plot in Fig. 18 the variation of the angles made with the horizontal axis  $x$ , of the free surface and the trajectories at a given instant. It is remarkable that the free surface and the trajectories have the same orientation at the two points 2 and 3. By superimposing the variation of  $s_y$ , we observe that at point 2,  $s_y$  vanishes and the orientation is  $\pi$ . At point 3, the angle of the trajectories with the horizontal axis is slightly greater than  $\pi$ . It is planned in future work to better analyse the possibility to associate the location of the maximum velocity with the fact that free surface and trajectories have the same tangent.

To set the basis of other future works, we examine the time variation of the fluid energy components. The potential and kinetic energies are plotted in Fig. 19. We first observe that the relative error on the energy conservation is rather acceptable, less than  $7 \cdot 10^{-4}$ . The main result is that the kinetic energy reaches a threshold, meaning that the accumulation of kinetic energy is bounded. To capture more critical plunging jets, it is expected that more kinetic energy must be stored by the fluid.

In the present case, the kinetic energy (nil at initial time of the simulation) originates from a continuous transfer from the initial potential energy. The latter being not sufficient, we have to increase more rapidly the amount of kinetic energy stored by the fluid.

One way to generate highly energetic wave is to create focused wave as performed in the SLOSH project, which is described in Brosset et al. [3,4] and Brosset et al. [2]. That means that a wavemaker is necessary or alternatively a preliminary wave train

is used as an initial condition, the latter being possibly computed from a Boussinesq approach as done earlier in [15]. Both approaches are avoided for the sake of computational resource savings. To this end, we operate in a sloshing tank. That approach has the advantages to be repeatable in laboratory.

## 5 Conclusion

In this paper, we have confirmed some results regarding the location of maximum velocity and acceleration. In addition, we propose simple formulae that can approximate the velocity field in the plunging jet. These properties can be generalized provided the plunging breaker develops in shallow water. Further investigations could be made to generalize the obtained formulae in deep water.

In future works, we shall examine how the fluid kinematics can be disturbed when greater amount of kinetic energy is injected in the fluid. Preliminary results are already shown in Socolan [23] and Socolan and Etienne [24]. In particular, we expect that critical jets may appear at the free surface in the barrel in the vicinity of the points where the velocity is the greatest.

### A. Brief Description of the Numerical Method

The numerical model is based on the potential theory. The free surface is an isobar and material line. The free surface is described with a finite number of markers with cartesian coordinates  $\vec{X} = (X, Y)$  that are tracked over time. The velocity potential is transported in a Lagrangian way on those markers with the fluid velocity  $\vec{\nabla}\phi$  computed at the same markers. The free surface boundary conditions are written in a Lagrangian way as follows:

$$\begin{cases} \frac{d\phi}{dt} = \frac{1}{2} \left( \vec{\nabla}\phi \right)^2 - gY \\ \frac{d\vec{X}}{dt} = \vec{\nabla}\phi \end{cases} \quad (4)$$

This differential system is solved using a standard Runge–Kutta of fourth order (RK4) that updates the velocity potential  $\phi_{fs}$  at the free surface. The velocity potential verifies the following boundary value problem:

$$\begin{cases} \Delta\phi = 0 & \text{in the fluid domain} \\ \phi = \phi_{fs} & \text{on the free surface} \\ \phi_{,n} = 0 & \text{on the fixed wall of the tank} \end{cases} \quad (5)$$

The method is desingularized in the sense that the velocity potential follows from the influence of a finite number of sources (Rankine–Green function) located outside the fluid domain. The number of sources and markers being the same, there is square linear system between the velocity potential computed at the markers and the strengths of the influencing sources. Using a conformal mapping that maps the inner tank domain

onto a half plane or a quarter plane, the homogeneous Neumann boundary condition on the walls can be implicitly accounted for in the expression of the Green function using images of the sources with respect to the axes. The unknowns of the problem are the velocity potential calculated at the moving markers.

The energy and mass conservations are checked at each step of the time integration. The time step is adapted to the speed of the simulated fluid motion. When the plunging breaker develops, the time step must decrease substantially. In all the computations done in the present paper, the relative errors on the mass and energy conservations are never greater than  $10^{-6}$  and  $10^{-3}$ , respectively. The number of markers/sources is set to few hundreds depending on the smoothness of the free surface, it does not vary over a given simulation. No smoothing is required. Regridding can be performed when the free surface is barely distorted. A natural concentration of markers occurs where and when it is necessary. That is the case in the plunging crest where the convection velocity is the greatest. Apart from the time step and the number of Lagrangian markers, the only arbitrary parameter is the distance of desingularization. It is chosen in the range of 2 and 3 times the distance between a given a marker and its two neighbour markers as proposed by Cao et al. [5]. It is shown that this choice optimizes the conservations of mass and energy.

The elaborated software has been continuously validated since its first development in 2007. Recently, the present code has been used for the benchmark organized in the frame of the Joint Collaborative Project TANDEM (Tsunamis in the Atlantic and the English ChanNel: Definition of the Effects through numerical Modeling). The present code yielded the reference data that describe the multiple reflections of a wave train in channel of 30 km long with a water depth 50 m (2500 markers are used). The results of Navier–Stokes solvers, Boussinesq solvers and potential solvers were benchmarked (see [1]). Another recent validation test focused on the energy distribution during the highly nonlinear sloshing in a tank of a two fluid system. Several sizes of entrapped gas pocket and flip-through configurations are treated (see [10]). The results of a Navier–Stokes solver and the present code show the limit of those approaches in terms of compressibility of the gas which should be accounted for depending on the shape of the entrapped gas pocket.

## References

1. Benoit, M., Dias, F., Herterich, J., Scolan, Y.-M.: A benchmark for the simulation of the propagation and run-up of wave train of tsunami type. (in french) Proc. des 16èmes Journées de l’Hydrodynamique, Marseille, France (2018)
2. Bogaert, H., Leonard, S., Brosset, L., Kaminski, M.L.: Sloshing and scaling: results from the SLOSHEL project. In: Proc. ISOPE, Beijing, China (2010)
3. Brosset, L., Mravak, Z., Kaminski, M., Collins, S., Finnigan, T.: Overview of SLOSHEL project. In: Proc. ISOPE, Osaka, Japan (2009)
4. Brosset, L., Lafeber, W., Bogaert, H., Marhem, M., Carden, P., Maguire, J.: Mark III panel subjected to a flip-through wave impact: results from the SLOSHEL project. In: Proc. ISOPE, Maui, Hawaii, USA (2010)
5. Cao, Y., Schultz, W.W., Beck, R.F.: A three-dimensional desingularized boundary integral method for potential problems. Intl. J. Numer. Methods Fluids **11**, 785–803 (1991)
6. Constantin, A.: The time evolution of the maximal horizontal surface fluid velocity for an irrotational wave approaching breaking. J. Fluid Mech. **768**, 468–475 (2015)

7. Constantin, A.: Nonlinear Water Waves with Applications to Wave-Current Interactions and Tsunamis, CBMS-NSF Reg. Conf. Ser. Appl. Maths, vol. 81. SIAM (2011)
8. Dold, J.W., Peregrine, D.H.: An efficient boundary-integral method for steep unsteady water waves. In: Morton, K.W., Baines, M.J. (eds.) Numerical Methods for Fluid Dynamics. Oxford University Press, Oxford (1986)
9. Dommermuth, D.G., Yue, D.K.P., Lin, W.M., Rapp, R.J., Chan, E.S., Melville, W.K.: Deep-water plunging breakers: a comparison between potential theory and experiments. *J. Fluid Mech.* **189**, 423–442 (1988)
10. Etienne, S., Scolan, Y.-M., Brosset, L.: Numerical simulation of highly nonlinear sloshing in a tank due to forced motion. In: Proc. of 37th International Conference on Ocean, Offshore and Arctic Engineering, Jun 2018, Madrid, Spain, pp. 2018–78624 (2018)
11. Guilcher, P.-M., Jus, J., Couty, N., Brosset, L., Scolan, Y.-M., Le Touzé, D.: Simulations of breaking wave impacts on a flat rigid wall Part 1: influence of the wave shape. In: Proc. of the 24th Int. Offshore and Polar Eng. Conf. (ISOPE), Busan, South-Korea, vol. 3, pp. 232–245 (2014)
12. Guyenne, P., Grilli, S.T.: Numerical study of three-dimensional overturning waves in shallow water. *J. Fluid Mech.* **547**, 361–388 (2006)
13. John, F.: Two-Dimensional Potential Flows with a Free Boundary. Communications on pure and applied mathematics, VI, pp. 497–503 (1953)
14. Karimi, M.R., Brosset, L., Ghidaglia, J.-M., Kaminski, M.L.: Effect of ullage gas on sloshing, part I: global effects of gas-liquid density ratio. *Eur. J. Mech. B/Fluids* **53**, 213–228 (2015)
15. Kimmoun, O., Malenica, Š, Scolan, Y.-M.: Fluid structure interactions occurring at a flexible vertical wall impacted by a breaking wave. In: Proceedings of the Nineteenth International Offshore and Polar Engineering Conference Osaka, Japan, pp. 308–315 (2009)
16. Longuet-Higgins, M.S., Cokelet, E.D.: The deformation of steep surface waves on water. 1. A numerical method of computation. *Proc. R. Soc. Lond. A* **364**, 1–26 (1976)
17. Longuet-Higgins, M.S.: A technique for time-dependent free-surface flows. *Proc. R. Soc. Lond. Ser. A Math. Phys. Sci.* **371**, 441–451 (1980)
18. Miller, R. L.: Role of vortices in surf zone prediction: sedimentation and wave forces. In: Davis, R.A., Ethington, R.I. (eds.) Beach and Nearshore Sedimentation. SOCE. con. Paleontologists and Mineralogists Spec. Publ. 24., vol. 14, pp. 92–1 (1957)
19. New, A.L., McIver, P., Peregrine, D.H.: Computations of overturning waves. *J. Fluid Mech.* **150**, 233–251 (1985)
20. Scolan, Y.-M.: Some aspects of the flip-through phenomenon: a numerical study based on the desingularized technique. *J. Fluid Struct.* **26**(6), 918–953 (2010)
21. Scolan, Y.-M., Karimi, M.R., Dias, F., Ghidaglia, J.-M., Costes, J.: Highly nonlinear wave in tank with small density ratio. In: Proc. 29th International Workshop on Water Waves and Floating Bodies, Japan, pp. 181–184 (2014)
22. Scolan, Y.-M., Brosset, L.: Numerical simulation of highly nonlinear sloshing in a tank due to forced motion. *Int. J. Offshore Polar Eng. (IJOPE)* **27**(1), 11–17 (2017)
23. Scolan, Y.-M.: Critical free surface flows in a sloshing tank. In: Proceedings of the 8th International Conference on Hydroelasticity in Marine Technology, Seoul, Korea, pp. 11–19 (2018)
24. Scolan, Y.-M., Etienne, S.: Critical jets in a breaking wave (in French). In: Proc. des 16èmes Journées de l’Hydrodynamique, Marseille, France (2018)
25. Skyner, D.: A comparison of numerical predictions and experimental measurements of the internal kinematics of a deep-water plunging wave. *J. Fluid Mech.* **315**, 51–64 (1996)
26. Song, B., Zhang, C.: Boundary element study of wave impact on a vertical wall with air entrapment. *Eng. Anal. Bound. Elem.* **90**, 26–38 (2018)
27. Tuck, E.O.: Solution of Nonlinear Free-Surface Problems by Boundary and Desingularised Integral Equation Techniques, Invited Lecture, Computational Techniques and Applications: CTAC’97 Eds J. Noye, M. Teubner, A. Gill, World Scientific, Singapore, pp. 11–26 (1998)
28. Vinje, T., Brevig, P.: Numerical simulation of breaking waves. *Adv. Water Resour.* **4**, 77–82 (1981)
29. Yasuda, T., Mutsuda, H., Mizutani, N.: Kinematics of overturning solitary waves and their relations to breaker types. *Coast. Eng.* **29**(3–4), 317–346 (1997)